Journal of Materials Research and Technology 42 (2026) 10907–10920

Contents lists available at ScienceDirect

Journal of Materials Research and Technology

journal homepage: www.elsevier.com/locate/jmrt

Mechanical properties of high-speed tool steel recycled from grinding chips by field-assisted sintering

Michelle Treppmann [a,*], Felix Großwendt [a], Monica Keszler [b], Martin Bram [b], Anna Assmann [c], Sebastian Weber [a]

[a] Lehrstuhl Werkstofftechnik, Ruhr-Universität Bochum, Universitätsstr. 150, 44801, Bochum, Germany
[b] Forschungszentrum Jülich, Wilhelm Johnen Str., Jülich, Germany
[c] Lehrstuhl für Anthropogene Stoffkreisläufe, RWTH Aachen, Wüllnerstr. 2, 52062, Aachen, Germany

ARTICLE INFO

Keywords:
Direct recycling
Tool steel
Grinding waste
Field-assisted sintering technology (FAST)
Mechanical properties

ABSTRACT

In the metal working industry, masses of grinding waste are generated every year that are disposed by landfill or combustion. In order to establish a circular economy, the recovery of the subtracted metallic portion is crucial. In particular, the introduction of high-alloyed tool steel chips as a secondary raw material for powder metallurgical processes is of interest from an economical and ecological point of view. Since the grinding waste consists not only of metallic chips but also of cooling lubricant and non-metallic abrasive particles, separation of the metallic grinding chips from the contaminations is a prerequisite for the recycling of the steel. Cleaned high-speed tool steel grinding chips that still contain non-metallic particles were compacted to cylindrical discs by field-assisted sintering technology (FAST). The residual non-metallic inclusions give rise to concerns regarding the mechanical properties of the recycled steel. Therefore, mechanical properties of the FAST-recyclate in heat-treated condition were assessed by static compression testing, pressure swelling testing, and cyclic bending testing. The resulting static and cyclic mechanical properties are compared to reference samples conventionally produced by hot isostatic pressing of pristine gas atomized powder. It was found that the static compressive properties of the recycled tool steel do not deviate significantly from those of the reference material. However, residual non-metallic inclusions lead to premature failure during both cyclic testing.

1. Introduction

To ensure wear resistance and strength at elevated temperatures high-speed tool steels (HSS) are alloyed with elements like W, Mo, V, and Co that are regarded critical by the European Union (EU) due to supply risks [1–4]. The supply risk for such elements became apparent in December 2024 when the PR China banned the export of W to the USA [5]. The elements V and Co also carry a high supply risk, as the PR China is the main supplier of V and the DR Congo, which is considered politically unstable, mines most of the available Co. Furthermore, Co demand is rising due to its use in battery technology which is a key technology for the advancing energy transition away from fossil fuels [1,2].

Currently, up to 2/3 of the produced HSS is removed by grinding processes during tool production. The removed steel chips form a sludge with the used cooling lubricants and abrasives, which is subjected to landfill or combusted. In Germany alone, more than 250 kt of grinding sludge is produced every year [6,7]. Additionally, high costs are incurred when disposing the environmentally hazardous grinding waste which contain high amounts of oils [8,9]. Instead of disposing the grinding waste, recycling it would be a much more environmentally friendly option. It would also assist in minimizing the production of the primary raw materials, which require high amounts of energy for production and cause environmental damage through emissions. Thereby, the valuable alloying elements contained in the metallic grinding chips can be reclaimed paving the way for a circular economy in the metal working industry.

For these reasons, two driving forces to recycle high-alloyed grinding waste arise: an economic driving force and an ecologic driving force. The economic reasons include the avoidance of disposal costs and the weakening of geopolitical dependencies regarding raw material supply chains [2,10–12]. The ecologic driving force is to avoid disposal hazardous waste, which also leads to less demand for primary resources. This would reduce the demand for energy intensive and environmentally destructive mining [1,2,4,8].

* Corresponding author.
E-mail address: m.treppmann@wtech.rub.de (M. Treppmann).

https://doi.org/10.1016/j.jmrt.2026.05.278
Received 30 July 2025; Received in revised form 20 April 2026; Accepted 25 May 2026
Available online 28 May 2026
2238-7854/© 2026 The Authors. Published by Elsevier B.V. This is an open access article under the CC BY license (http://creativecommons.org/licenses/by/4.0/).

The EU aims to implement the United Nations' (UN) Sustainable Development Goals by reducing economic and ecological dependencies and supporting the transition to environmentally sustainable development [2,11]. Recycling high-alloyed grinding chips would bring them one step closer. Two of the sustainable development goals of UN are addressed by the recycling approach for grinding waste presented in this work, goal 9 “Industry, innovation and infrastructure” and goal 12 “Responsible consumption and production”. The aim is to switch to resource-efficient and climate-friendly production and to transition from a linear economy to a circular economy [13].

A promising approach for recycling of grinding chips is the usage of the chips as starting powder for powder metallurgy (PM), as grinding chips can already be considered a powder-like material [14,15]. Using PM as a direct recycling technique eliminates the need to remelt and subsequently either atomize or cast the waste material, which can contribute to energy savings during production [15,16]. However, a prerequisite for the direct recycling of grinding chips by PM is the separation of the metallic chips from contaminating cooling lubricant and abrasive particles [17]. Otherwise, residual oil can evaporate or burn at high temperatures making the sintering of the metallic powder more difficult [18]. Furthermore, it is assumed that the residual oils or binders could lead to C and H uptake during sintering of the metallic chips, which in turn influences the materials' properties. Additionally, residual non-metallic abrasive particles may reduce the toughness of the recycled material. In addition, certain abrasives like SiC are known to dissolve in Fe-base alloys during sintering, which leads to further changes in the chemical composition [18].

Several ways to separate metallic chips from oil and abrasives are reported in literature. Deoiling can be performed by means of supercritical fluid extraction using carbon dioxide (CO_2) for example. However, re-precipitation of oil has been reported if the grinding waste contains a high proportion of oil, as oil is only soluble to a limited extent in supercritical CO_2 [18]. Fu and Matthews concluded that, from an economic point of view, deoiling of grinding waste by supercritical CO_2 is not competitive [17]. Another option is to remove the oil by washing with liquid media such as aqueous surfactant solutions or organic solvents such as acetone. Since the considered high-speed tool steel is not corrosion-resistant, oil removal by acetone is used in this work to limit oxidation of the metal chips during cleaning [17,19]. Otherwise, oxides could affect the sintering of the metallic chips and reduce the toughness of the recycled material [20].

After cleaning of the grinding chips, direct recycling by PM is still challenging. The spiral morphology of grinding chips promotes interlocking of particles and thus leads to low apparent powder packing density. Preliminary studies demonstrated that direct recycling by hot isostatic pressing (HIP) results in uncontrolled shrinkage and deformation of the used container. Even an upstream ball milling step could not improve the apparent density of the grinding chips to an extent that HIP could be performed successfully [7,20]. To overcome the low apparent density of grinding chips, pressure and field-assisted sintering technology (FAST) is a promising approach [21,22]. Another benefit of sintering by FAST is the much lower sintering times compared to HIP and conventional sintering techniques, which can lead to a comparative saving in energy consumption and operation costs [23–25].

The goal of this work is to recycle the metallic swarf of HSS AISI PM T15 by sintering using FAST to form discs. The disc will be used to produce cutting tools. Prior to sintering by FAST, a three-stage preparation including washing in organic solvent, vacuum filtration, and planetary ball milling is performed. Disc-shaped samples of 120 mm diameter and 3 mm thickness are subjected to an adapted heat-treatment that takes the chemical compositions altered by contaminations into account. The samples are characterized regarding microstructure evolution as well as the static and cyclic mechanical properties. These results are compared to the PM T15 reference material which was conventionally produced by HIP of gas atomized powder.

The following scientific questions will be clarified in this work:

- Is FAST suited to produce dense components from the considered aspherical HSS grinding chips?
- How can the typical heat-treatment of PM T15 be adapted to the FAST-recyclate, which is likely to exhibit an altered chemical composition due to contaminants, in order to achieve similar mechanical properties to the reference material?
- How do the microstructures that emerge from FAST deviate from the microstructure of the conventional produced reference material?
- How do the microstructures of the FAST-processed recyclate that contain non-metallic inclusions impact the static and cyclic mechanical properties of the samples?

2. Materials and methods

2.1. Materials used

The considered grinding waste was generated during the manufacturing of broaches. Broaches require exceptional compressive strength and wear resistance, as well as sufficient toughness to withstand stress peaks without cracking, which are produced from PM HSS AISI PM T15 (DIN 1.3251, PM HS12-0-5-5) (Table 1).

The PM T15 is also commonly used for mold cutters, end mills, and shear blades. The grinding of the broaches takes place in two steps. The tool profile is created in soft annealed condition by grinding with coarse Al_2O_3 grinding wheels. To ensure the geometric tolerances and to sharpen the tool after hardening and tempering, a final grinding step using a cubic boron nitride (cBN) grinding wheel with a finer grain size is conducted. The grinding waste is therefore contaminated with Al_2O_3 and cBN abrasive particles. Both types of grinding wheels are polymer bonded. To reduce the wear of the grinding wheels, a water-free cooling lubricant oil is applied in both grinding steps.

The first step in deoiling of the grinding sludge is deagglomeration. Deagglomeration is carried out using a liquidizer equipped with Cr-steel blades. 1.5 kg of grinding sludge are deagglomerated for 10 min at 5000 rpm. Otherwise, large agglomerates could promote an imbalance during the subsequent centrifugation causing an emergency stop of the centrifuge. 350 g batches were centrifugated for 10 min at 2500 rpm. Thereby a 1 mm mesh inlay was used to sperate the cooling lubricant and the swarf. Afterwards, a washing with acetone is conducted using a 1:1 mass ratio and mixing until homogeneity. Thereby, agglomerates reformed during centrifugation were broken up so that the exposure of the individual grinding chips to the solvent is promoted. Afterwards, the loaded solvent was separated via vacuum filtration. As a result, the total carbon content measured by carrier gas hot extraction was reduced from an initial value of 25.5 ± 2.5 mass% to 1.7± 0.1 mass%. The spiral shape of the deoiled grinding chips is then broken down through milling batches of 50 g at 710 rpm for 3 min using a disc swing mill equipped with WC milling works. The preparation procedure increases the apparent density of the grinding waste from 0.4 g/cm^3 to 2,21 g/cm^3. Simultaneously, the average particle size d_{50} is reduced from 58 to 36 μm. Further information regarding the preparation of the grinding waste can be found here: [26]. After the performed deoiling, the steel is still contaminated with <1 vol% of Al_2O_3 and cBN abrasive particles. The impact on the compressive strength, the critical load above which cracks form and the crack growth rate of the reclaimed steel will be investigated.

The obtained steel powder was characterized by dynamic image analysis using the QICPIC system (Sympatec, Germany). The chemical composition of the grinding chips as well as that of the bulk samples was determined by XRF using a type XL2 air (Thermo Fisher, USA). The content of the light elements C, N, and O was determined by carrier gas hot extraction using elemental analyzers of type CS-800 and ONH-2000 (Eltra, Germany).

2.2. Production of bulk samples by FAST and conventional processing

The different processing routes of the recyclate and the reference

Table 1
Nominal chemical compositional range, chemical composition of reference, of the recyclate powder, and actual chemical composition of the recyclate produced by FAST of PM T15 in mass% (measured by XRF except for light elements which were measured by carrier gas hot extraction).

	C	Mn	Si	Cr	Mo	V	W	Co	Al	N	B	O
Nominal	1.50 – 1.60	0.10 – 0.40	0.10 – 0.60	3.70 – 4.50	<1.00	4.50 – 5.30	11.70 – 13.00	4.70 – 5.30	–	–	–	–
Reference	1.59 ± 0.01	0.33 ± 0.00	0.50 ± 0.14	4.32 ± 0.05	0.48 ± 0.03	4.74 ± 0.06	12.09 ± 0.02	4.91 ± 0.11	<0.001	0.09 ± 0.01	–	0.01 ± 0.00
Recyclate powder	1.70 ± 0.10	0.33 ± 0.01	0.39 ± 0.01	4.91 ± 0.06	0.51 ± 0.01	5.09 ± 0.03	12.38 ± 0.06	5.07 ± 0.03	0.04 ± 0.02	0.12 ± 0.02	0.02 ± 0.01	0.44 ± 0.03
FAST	1.77 ± 0.01	0.33 ± 0.03	0.61 ± 0.06	4.00 ± 0.08	0.74 ± 0.00	4.57 ± 0.05	11.75 ± 0.07	4.88 ± 0.03	0.09 ± 0.01	0.12 ± 0.01	0.02 ± 0.02	0.54 ± 0.02

material are depicted in Fig. 1. After the cleaning procedure of the grinding waste, the samples were compacted by field-assisted sintering technology (FAST) which is also known as spark plasma sintering (SPS). FAST is a low-voltage, current- and pressure-assisted short-time sintering process [27]. The FAST device (DSP515, Dr. Fritsch, Germany) is equipped with two graphite punches and a graphite die that allow the production of cylindrical specimens with a diameter of 120 mm as well as a pyrometer to measure the temperature at the punch. Energy consumption of the device was measured by a PEL 103 power and energy logger (Chauvin Arnoux Metrix, France). To achieve a thickness of 3 mm, 275 g of PM T15 grinding chips were filled into the die. The graphite die and punches are lined with a graphite foil to improve the contact and to support the ejection of the sintered samples. The foil is coated with BN spray to inhibit the reaction between the steel powder and the graphite. The graphite punches apply an external axial pressure of 45 MPa. The graphite punches and die, as well as the metallic powder, are simultaneously heated with a heating rate of 100 K/min to 950 °C by Joule heating caused by the electric current. In a preliminary study, it

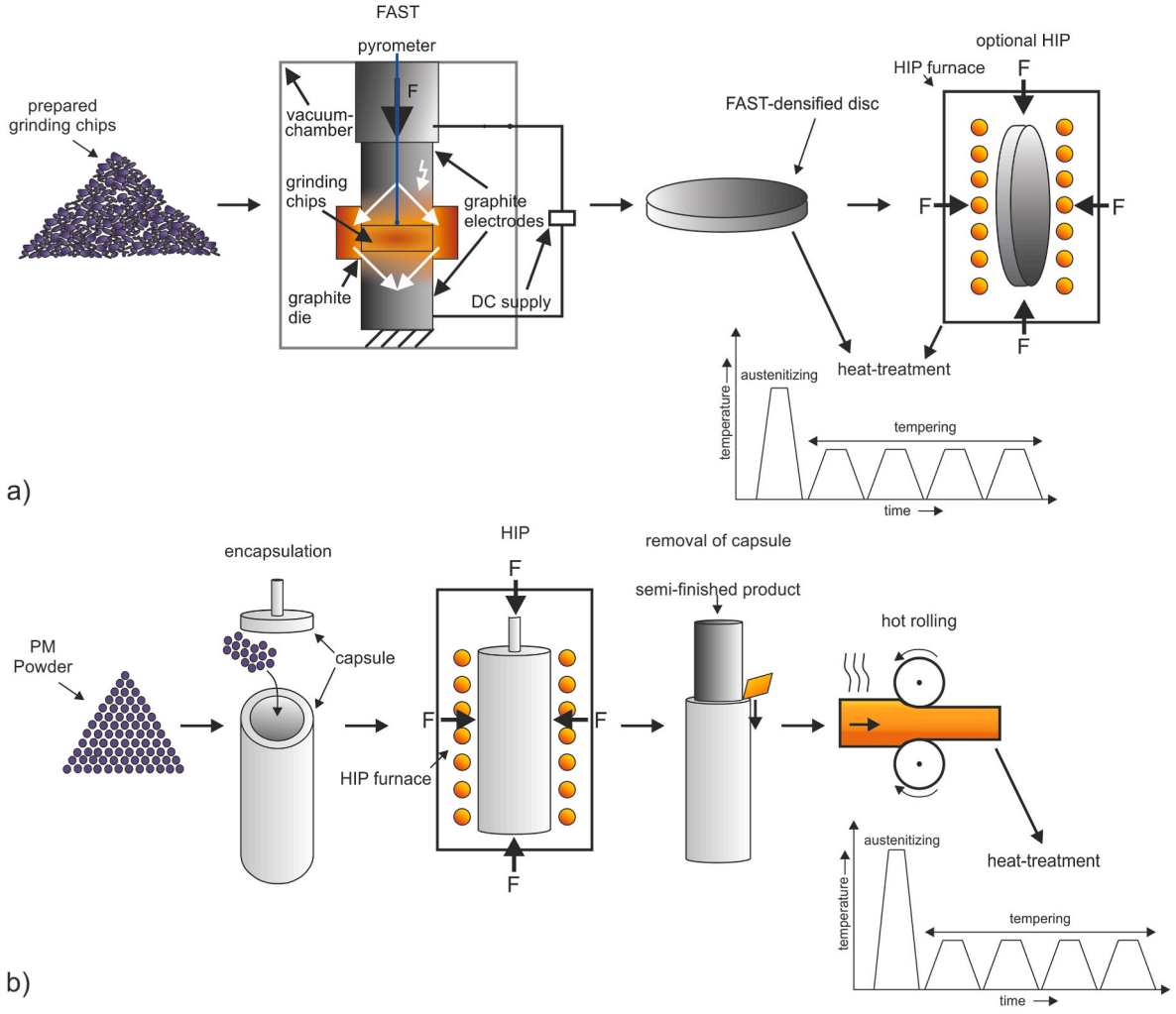


Fig. 1. Schematic depiction of a) sample production by direct recycling of the grinding chips by FAST and b) production of the reference material by conventional HIP processing route with subsequent hot rolling starting from commercial PM T15 powder.

was found that applying more than 50 MPa at temperatures above 1000 °C caused the sintered material to enter the gap between the punches and the die, resulting in the destruction of the tools during ejection. The superposition of pressure und electric current during FAST allows short sintering times of only a few minutes. Sintering times of 1 min and 5 min are examined. The FAST processing is schematically described in Fig. 1a.

To eliminate residual porosity within the FAST-processed samples, post-densification by container-less HIP was investigated. The post-densification by HIP was performed at 1150 °C under a pressure of 100 MPa in Ar atmosphere. The samples were compacted for 3 h in the HIP. Finally, a heat treatment consisting of austenitizing for 10 min in Ar atmosphere and oil quenching, followed by four times tempering for 2 h at 540 °C in a convection furnace, is performed.

Hereinafter, the samples will be labelled as follows. The reference samples are designated 'reference' and the samples made from FAST-densified grinding chips are designated 'FAST'. The samples additionally are indicated with a suffix. The suffix '1 min' refers to the dwell time at sintering temperature in the FAST device of 1 min, and the suffix '5 min' indicates the dwell time of 5 min. The suffix 'Q' corresponds to the heat-treatment condition "austenitized and quenched" and the suffix 'QT' indicates the heat-treatment condition "austenitized, quenched, and tempered in the regime of secondary hardness at 540 °C".

As a state of reference, commercial PM T15 bulk material is considered. This reference material was supplied by Böhler (Austria) and produced by HIP of N_2 gas atomized powder and subsequent hot rolling (Fig. 1b). The reference material was austenitized at 1215 °C for 10 min and subsequently oil quenched. Afterwards, tempering four times at 540 °C for 2 h was performed.

2.3. Thermodynamic calculations

Given that the uptake of C by the FAST-recyclate can result in the formation of excessive amounts of retained austenite (RA), the austenitizing temperature is adapted to accommodate the altered chemical composition of the recycled material. Therefore, the solute C content of the austenite phase is calculated using the Thermocalc (TC) version 2024a software (Thermocalc software AB, Sweden). Calculations were performed using the database TCFE10, considering the chemical compositions given by Table 1. The contents of B, N, O, and Al were neglected since no dissolution of the cBN and Al_2O_3 particles in the steel matrix could be observed. The considered phases are ferrite, austenite, MC, M_6C, M_7C_3, $M_{23}C_6$, cementite, and liquid.

2.4. Mechanical testing

Several testing methods were conducted to investigate the static and cyclic mechanical properties of the recycled material in comparison to the reference material. First, to produce the desired cutting disc from the FAST-densified disc, a ring was water jet-cut. The ring was fitted in a test rig for mechanized tunneling. The left-over inner disc was then used to cut out the samples for static and cyclic mechanical tests (Fig. 2a). The samples for the reference material were taken from a rolled flat steel strip in the direction longitudinal to the rolling direction (Fig. 2b).

Those samples were cut by electric discharge machining.

The samples underwent hardness testing, which was performed using a type KB-30s hardness testing device (KB Prüftechnik, Germany) according to DIN EN ISO 6507-1 (Vickers HV30) [28].

In addition, the static mechanical properties were investigated by compression tests according to DIN EN ISO 50106 [29]. The compression tests were conducted on the universal testing machine Z100 (ZwickRoell, Germany) with a testing speed of 0.5 mm/min. The

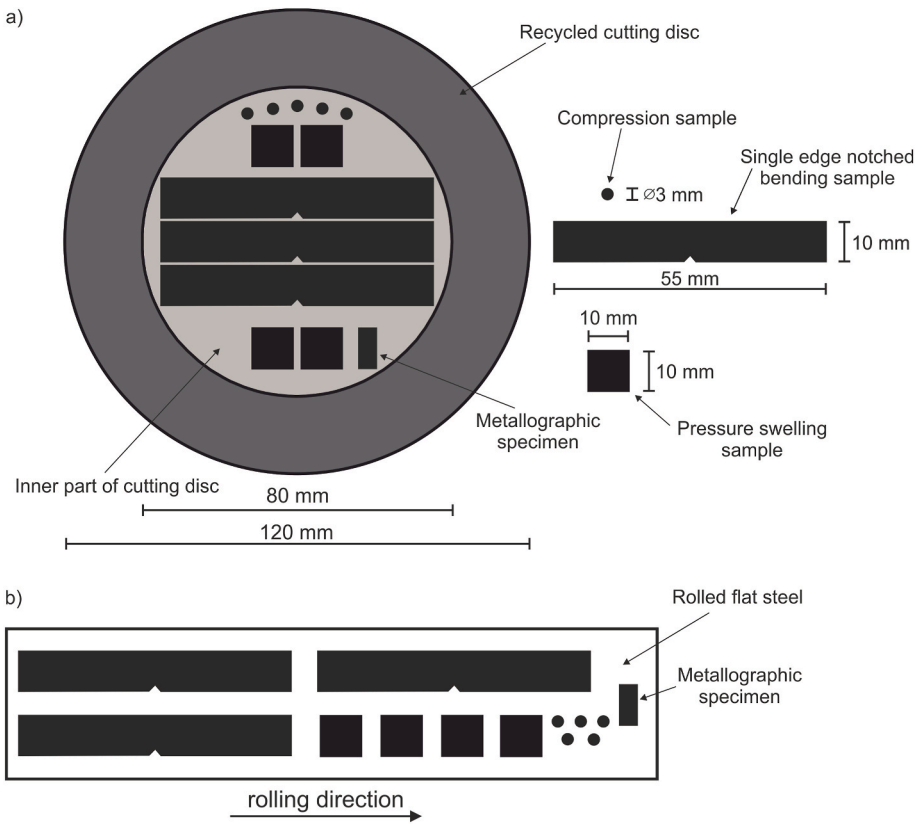


Fig. 2. Sampling plan for mechanical testing of a) the FAST-densified disc and b) the reference material. All samples have a height of 2.5 mm. The recycled cutting disc will be used for practical tool test.

average of five individual tests was calculated.

For cyclic mechanical testing, pressure swelling, and cyclic three-point bending tests were conducted. The cyclic mechanical tests were performed using the dynamic resonance testing machine type RUMUL Mikrotron 20 kN (Russenberger Prüfmaschinen AG, Switzerland).

Cyclic pressure swelling tests are carried out to identify the defects that cause cracks and to determine the critical load above which cracks form. The stress ratio R for the cyclic mechanical tests is $R = 0.2$. The radial local strain of the pressure swelling samples at the indent is calculated based on following formula: $\sigma = 0.5 \cdot (1 - 2 \cdot \nu) \cdot p_m$ with ν as the Poisson's ratio assumed to be $\nu = 0.3$. The local pressure p_m can be calculated as $p_m = A \cdot F_o$, with the top load F_o, and the area $A = \pi \cdot r^2$, where r is the radius of the indent of the ball-shaped Si_3N_4 ceramic counter body [30].

The subcritical crack growth is to be investigated according to ASTM E647-15 on pre-cracked single edge notched bending (SENB) samples, exhibiting a Chevron-notch [31]. The threshold value of subcritical crack growth as well as the crack growth rate, can be measured with an applied crack gage. The threshold value of subcritical crack growth was determined by automated increase of the stress intensity by 0.2 MPa $\cdot \sqrt{m}$ after every 100,000 cycles without measurable crack growth, starting from a value of 3 MPa$\cdot\sqrt{m}$. The termination criterion of the test was the failure of the sample.

The cutting discs were tested using the RUB-Tunneling Device (RUB-TD), a test rig designed to simulate mechanized tunneling (Fig. 3). In the test setup, the cutting discs were pressed against a counterbody made of sandstone with a static force of 2.5 kN. The test was conducted for a duration of 20 min at a rotational speed of 11.2 rpm. Further information regarding the test rig for mechanized tunneling can be found in the work of Brackmann et al. [32].

2.5. Metallography and microscopy

The relative densities of the FAST-densified discs were determined using the gravimetric method of density determination according to Archimedes with ethanol as the fluid medium.

For metallographic investigations, cross-sections of the samples were prepared by grinding with SiC abrasive paper from 320 to 1000 mesh, followed by polishing with diamond suspensions of grain sizes ranging from 9 μm to 1 μm. Investigation of the samples at high magnifications and energy-dispersive X-ray spectrometry (EDS) elemental maps were realized using a field-emission scanning electron microscopy (SEM) of type MIRA3 (Tescan, Czech Republic). The SEM operated at a working distance of 15 mm with an acceleration voltage of 20 kV using both secondary electron (SE) and backscatter electron (BSE) contrast. The usage of either SE or BSE contrast is specified in the captions of the SEM images. After the specimens had been tested under cyclic mechanical load, the correlation between microstructural features and the fracture load were established by quantitative image analysis using SEM micrographs (Fiji Distribution, National Institute of Health, USA) [33]. Thereby, the shape as well as the mean distance between large non-metallic inclusions were determined to draw conclusions about their influence at the stage of subcritical crack growth.

To determine the retained austenite (RA) contents of the samples in various heat-treatment conditions the X-ray diffractometer (XRD) type μx-360 (Pulstec, Japan) was used. The XRD was equipped with a Cr X-ray tube and a collimator of 2 mm diameter. During the measurement, full Debye ring profiles from a single incident X-ray angle were recorded and afterwards converted into intensity/2θ diagrams. The RA content is determined according to the Rietveld method considering the intensities of the martensitic/ferritic bcc and austenitic fcc phase reflections. The arithmetic mean of five measurements at various locations on each sample was documented.

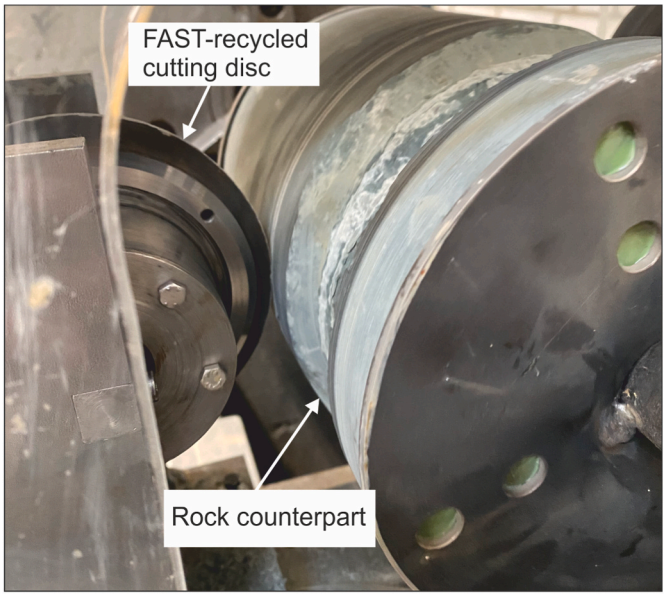


Fig. 3. FAST-recycled cutting disc installed in a test rig for simulation of mechanized tunnel construction.

3. Results and discussion

3.1. Starting powder properties

The recycled material is contaminated with residual cooling lubricant oil, the abrasive particles Al_2O_3 and cBN, and oxides, which formed during grinding due to reaction of the hot metallic chips with the oxygen in the atmosphere. Therefore, a chemical composition deviating from the reference composition is resulting, as detailed in Table 1. In addition, the composition varies between the batches of grinding waste that were supplied.

The particle sizes of the starting powder range from 2 μm to 800 μm as shown in Fig. 4a. The particle size distribution function q_3, which refers to the volume of the particles, appears multi modal with peaks at particle sizes of 45 μm, 430 μm and 680 μm. The coarser fractions observed can be associated with agglomerated sickle-shaped metal chips (particles of size above 400 μm). The characteristic values d10, d50, and d90 were determined to be 10 μm, 48 μm, and 592 μm respectively.

Fig. 4b shows a SEM image of the starting powder. The starting powder has a mixed morphology due to the two different grinding steps of the broaches. In the first grinding step, long spiral-shaped chips are generated due to the higher ductility of the soft annealed semi-finished tool. After the heat-treatment of the broach, the material is more brittle, thus the chips become shorter (Fig. 4b).

The prepared grinding chips exhibit an apparent density of 2.2 g/cm^3 and a tap density of 2.5 g/cm^3.

3.2. Densification and microstructure formation of the prepared grinding waste by FAST

Keszler et al. investigated the impact of the dwell time at sintering temperature during FAST densification of cold work tool steel grinding chips and found no improvement if dwell times exceeded 1 min [34]. Therefore, to save energy and minimize the processing time for the production of the recycled discs, an initial sintering time of 1 min at 950 °C was selected in this work. However, this results in an insufficient densification of the grinding chips. A relative density of the as-FAST state of 97 % (7.85 g/cm^3) in comparison to the reference material (8.08 g/cm^3) was measured. The presence of numerous large pores was observed as depicted in Fig. 5.

To increase the density and eliminate the residual porosity of the 1 min sintered disc, post-densification by container-less HIP was carried

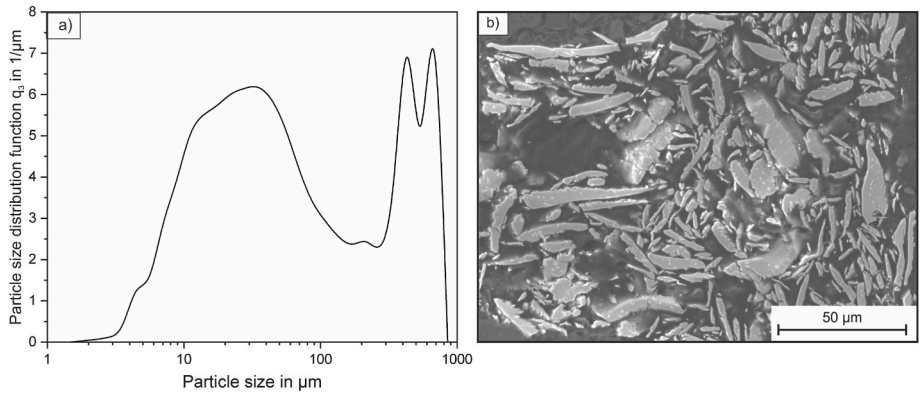


Fig. 4. a) Particle size distribution and b) SEM image in SE contrast of the starting powder.

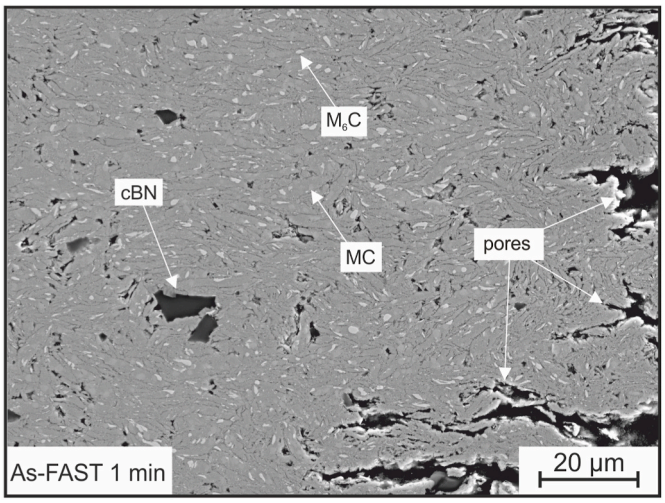


Fig. 5. Exemplary SEM image in SE contrast of the porosity in the as-FAST 1 min sample.

out. Due to inhomogeneous post-densification warping occurred.

To reduce the porosity of the FAST-densified disc, while avoiding further post-treatments, the sintering dwell was increased to 5 min. This resulted in a density of 8.05 g/cm^3 which resembles a relative density of 99.63 %. Compared to the FAST-produced samples using 1-min dwell time, the porosity was significantly reduced (compare Figs. 5 and 6). The recycled powder of PM T15 was contaminated with 0.2 vol% of Al_2O_3 and cBN abrasives, which both have less than half of the density of the steel chips and therefore impact the density measurement.

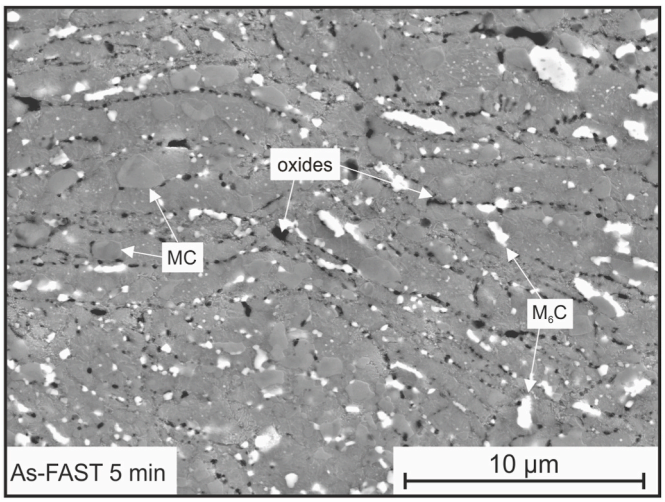


Fig. 6. Representative SEM micrograph in SE contrast of the as-FAST sample sintered for 5 min.

In contrast to the observations of Keszler et al., increasing of the sintering time led to an increase in density in this work [34]. It is assumed that this discrepancy originated from the upscaling of the samples in this study compared to the samples produced by Keszler et al. In this study, discs of 120 mm diameter and a weight of 275 g are produced while Keszler et al. manufactured samples of 20 mm diameter and 5 g weight. The larger samples require more time to be entirely heated to the desired sintering temperature. Insufficient dwell times in FAST are expected to lead to lowered temperatures at the center of the sample to be sintered. In addition, the increased number of particles results in higher friction, especially on the punch faces. This could result in less densification for the given punch pressure, which could only be compensated by a longer sintering time allowing for more diffusion.

With a fivefold increase in sintering time of 1 min to 5 min, the FAST device requires only approximately 30 % of additional energy during the FAST processing. This can be justified by the energy consumption which is dominated by the heating phase and not by the dwell time. The total sintering cycle with 5 min dwell time had an energy consumption of 16.8 kWh, whereas sintering for 1 min resulted in an energy consumption of 12.5 kWh. However, the post-densification by HIP after 1 min FAST needs to be considered as well. The energy consumption of the 1 min FAST-processed combined with the required post-processing (additional ~17 kWh for post-densification with HIP Quintus QIH9) is significantly higher than sintering for 5 min without post-densification. Therefore, a sufficient densification achieved by elongated FAST processing with no need for post-densification is preferable. Consequently, only the discs that have undergone sintering for a 5 min dwell time were subjected to further analysis.

The microstructure of the as-FAST 5 min sample is depicted in Fig. 6. The shape of the former grinding chips is still visible. In contrast to the 1 min dwell time (Fig. 5), the chips are surrounded by roundly molded oxides in between (Fig. 6).

Similar to the PM T15 reference material, V-rich carbides of type MC (dark contrast) and W-rich carbides of type M_6C (bright contrast) are embedded in the matrix. The MC are roundly molded but the M_6C are partly elongated due to deformation during the grinding process. As the M_6C have a lower elastic modulus than the MC, they are more sensitive to deformation and therefore appear more elongated and less spherical [35].

Fig. 7 displays the microstructure in a low magnification. The abrasives cBN and Al_2O_3 were irregularly distributed over the entire material. It can be clearly seen that most of the Al_2O_3 particles are significantly larger than the cBN particles (compare Table 2). As depicted in the elemental maps (quantified in mass%) in Fig. 7, the abrasives of type cBN and Al_2O_3 do not dissolve during the FAST

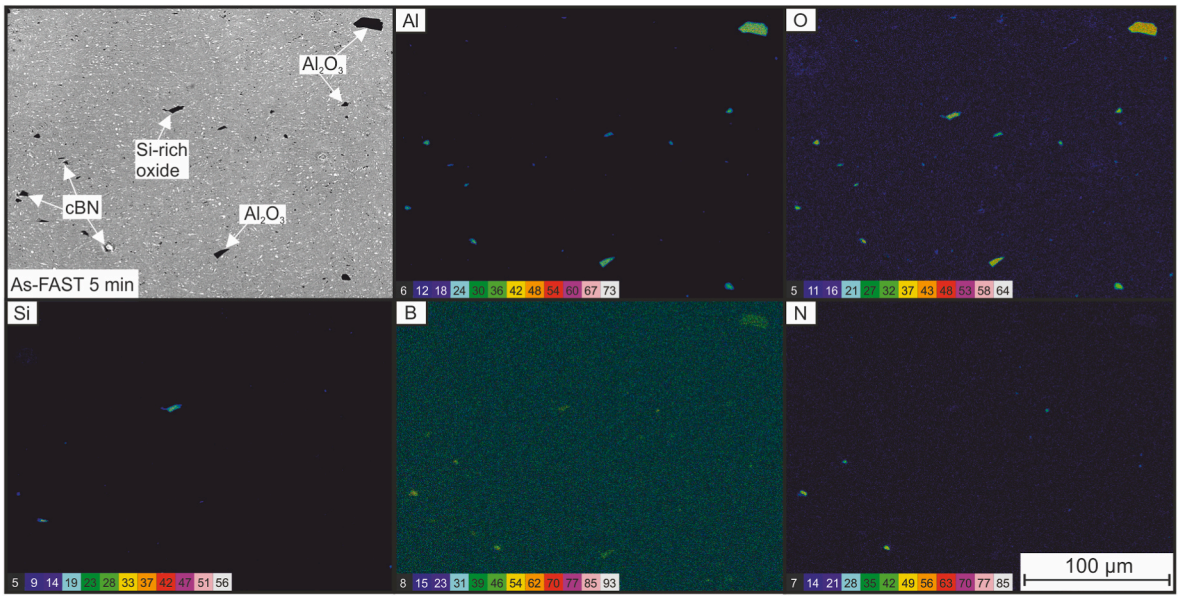


Fig. 7. SEM image in BSE contrast and selected elemental maps (quantified in mass%) of the contaminations of the FAST-densified recyclate.

Table 2
Morphology and distribution of the carbides, oxides, and contaminations in the reference material and in the FAST 5 min + QT recyclate.34.

		Volume fraction in %	Mean size in µm	Circularity	Mean interparticle distance in µm	Mean free matrix length in µm
Reference	M_6C	4.0	0.5 ± 0.3	0.8	21.5	13.2
	MC	7.5	0.6 ± 0.2	0.9	10.0	
	oxides	0.0	0.3 ± 0.2	0.9	2770.4	
FAST	M_6C	3.6	0.4 ± 0.3	0.8	31.6	6.4
5 min	MC	4.7	0.4 ± 0.3	0.8	21.6	
+ QT	oxides	1.6	0.2 ± 0.1	0.9	78.0	
	cBN	0.1	0.5 ± 0.7	0.8	3726.7	
	Al_2O_3	0.7	2.4 ± 1.7	0.3	61.9	

process. Further, the mapping revealed a Si- and O-rich phase which could be identified as a Si-rich oxide.

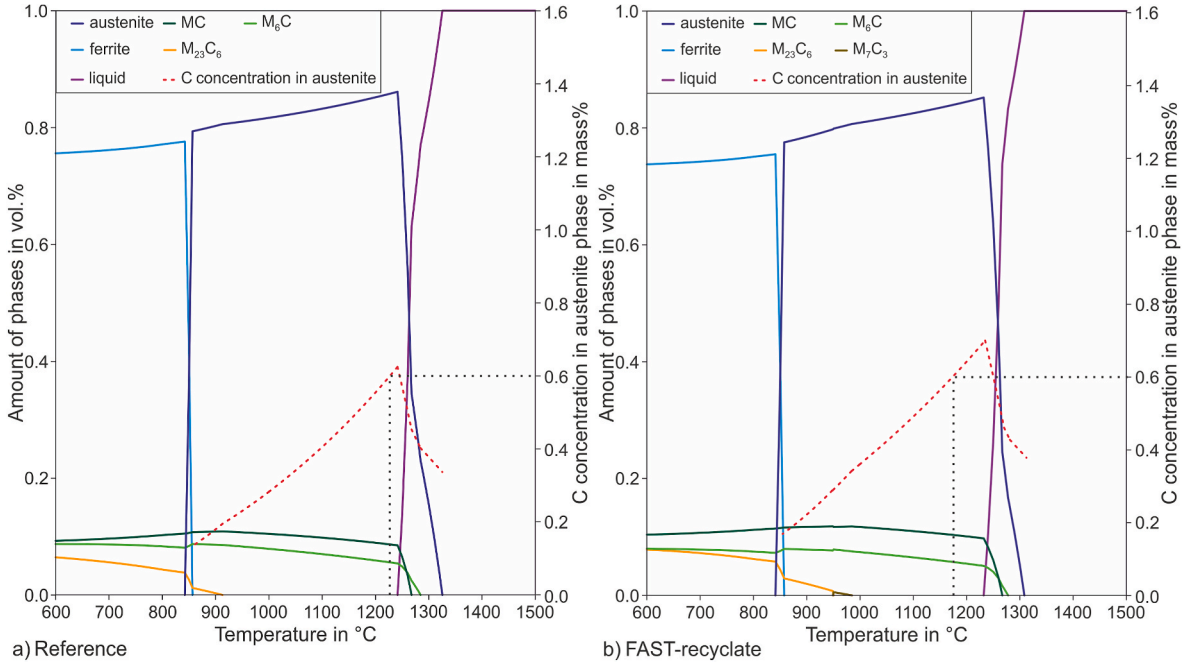


Fig. 8. Calculated phase fraction diagram and C concentrations in austenite phase with marked austenitizing temperatures of a) the reference and b) the FAST 5 min + QT.

3.3. Adapted heat-treatment of the FAST-recyclate

The heat-treatment of HSS consists of austenitizing close to the solidus temperature followed by quenching and tempering in the regime of secondary hardness multiple times [36]. A high hardness with simultaneously high toughness is prerequisite for the targeted applications.

Since the C content, which varies between the reference condition and the FAST-recyclate, greatly affects austenite stability and carbide formation, an adapted austenitizing temperature is required (Table 1). Otherwise, excessive solute C concentration during austenitizing would result in excessive RA content, which would reduce the hardness.

Fig. 8 shows the calculated phase fraction diagram including the solute C concentration in austenite phase of both, the reference and the FAST-densified recyclate.

The global C content of the FAST-processed recyclate is increased due to C uptake associated with decomposition of residual cooling lubricant and a slight C diffusion from the graphite foil, which can occur if the BN coating of the foil is cracked. Therefore, the solute C concentration in austenite phase of the recycled material is increased compared to the reference material (compare Table 1 and Fig. 8). At the austenitizing temperature of the reference material of 1215 °C, 0.67 mass% C mass is in solute, rather than the expected 0.6 mass%. Since solute C contents of more than 0.6 mass% are known for promoting excessive retention of austenite after quenching, an adapted austenitizing temperature must be applied to the FAST-recyclate. To achieve the same solute C concentration of 0.6 mass% in austenite phase as in the reference state, the austenitizing temperature needs to be reduced to 1170 °C according to the calculations. Besides promoting excessive RA contents, the increased C content of the recycled material reduces the solidus temperature. Therefore, if the same austenitizing temperature as of the reference material would have been applied to the FAST-recyclate, the material would have surpassed the solidus temperature, thus partially melting would occur. Partial melting would lead to the formation of eutectic carbide networks decreasing the toughness and could also result in shape-loss of the near-net shape disc [37–39]. Therefore, surpassing the solidus temperature during heat-treatment must be avoided.

The resulting hardness and the RA content of the reference material, of the FAST-recyclate (as-FAST), of the FAST-recyclate which has undergone austenitizing at 1170 °C with subsequent quenching (FAST + Q), and of the FAST-recyclate which was austenitized at 1170 °C with subsequent quenching and additional tempering (FAST + QT) are shown in Fig. 9.

It should be noted that the RA contents measured with XRD are generally overestimated for steels with a high content of V-rich MC, such as PM T15. This is because the reflections of V-rich MC and austenite, which both exhibit fcc crystal structure can hardly be distinguished.

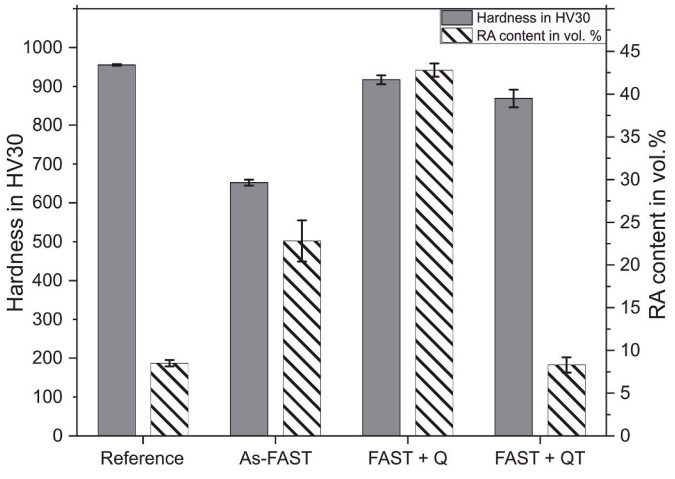


Fig. 9. Hardness in HV30 and the retained austenite content in vol% of the reference material and the FAST-recyclate in varying heat-treatment conditions.

The reference sample exhibits a hardness of 955 ± 2 HV30 and a RA content of 8.5± 1 vol% (Fig. 9). In the as-FAST condition, a hardness decrease of approx. 300 HV30 and a significantly increased RA content in comparison to the reference material are observed (Fig. 9). The lower hardness is attributed to the comparably low sintering temperature of 950 °C and the reduced cooling rate compared to oil quenching. According to the calculations shown in Fig. 8, only 0.3 mass% C is solute in the austenite phase at 950 °C. This is what led to the decreased hardness compared to FAST + Q. The adapted austenitizing temperature of 1170 °C for the FAST-recyclate led to an initial hardness above 900 HV30 and a RA of 43 % (Fig. 9). Austenitizing at a higher temperature compared to FAST processing (950 °C) increased the dissolution of carbides resulting in an increased solute C content (compare Fig. 8). Further, the higher thermal activation during austenitizing compared to FAST led to increased C diffusion and a more homogeneous distribution of C. As the solute C stabilizes the austenite phase, more RA remains after hardening (FAST + Q) than after FAST processing (Fig. 9).

After tempering, the hardness of FAST + QT was slightly decreased but achieved nearly the same RA content as the reference material (Fig. 9). Due to the multiple tempering in the regime of secondary hardness of FAST + QT, RA is transformed into martensite and tempering carbides. Thus, the RA content is significantly lowered compared to both as-FAST and FAST + Q conditions. However, residual porosity led to a slightly lower hardness compared to the reference material. The porosity as well as the remaining abrasive particles also result in an increased scatter in the measured hardness values compared to the reference material (Fig. 9).

The microstructures of the PM T15 reference material and the FAST 5 min + QT sample are depicted in Fig. 10. Both samples exhibit carbides of type MC (V-rich) and M_6C (W-rich) which are embedded into a tempered martensitic matrix. It is evident that there are more oxides present in the recycled material. The distribution of the oxides gives indications of the former shapes of the grinding chips. As was also observed prior to the heat-treatment, the MCs have a round morphology while the M_6Cs are still partly elongated in the recycled material (Fig. 10b).

During the heat-treatment, Al_2O_3 and cBN remain inert. The abrasive particles can be distinguished from the oxides by their size and shape. Since the morphology and the distribution of the hard phases influences the mechanical properties of tool steels, image analysis was conducted to quantify the characteristics of the observed phases in the reference material and the FAST 5 min + QT sample. Table 2 displays the volume fractions, the morphologies, and the distribution of the carbides, oxides, and contaminations determined by image analysis [33]. The carbides of the FAST 5 min + QT sample are smaller than those in the reference material due to the former grinding process. Furthermore, the circularity of the carbides in the FAST 5 min + QT sample is decreased. Since the FAST 5 min + QT sample is contaminated with Al_2O_3 and cBN particles, the volume fractions of contained hard phases differ from the reference material. Compared to the carbides and the cBN abrasive particles, the Al_2O_3 particles contained in the FAST 5 min + QT sample exhibit drastically decreased circularity. Due to an increased content of oxides, and the presence of abrasive particles, the free matrix path length of the recycled material is reduced by half compared to the reference material.

3.4. Static and cyclic mechanical properties of the heat-treated FAST-recyclate

The mechanical properties under static and cyclic loading are of particular interest because typical applications, e.g. as forming or cutting tools, subject the material to severe mechanical loads and rapidly changing load amplitudes [40]. Since the aim of this work is to evaluate if the FAST-recyclate can be used as a recycled tool, the compressive yield strength, the compressive strength, and the stress where an incipient crack is formed, as well as the crack growth rate, are

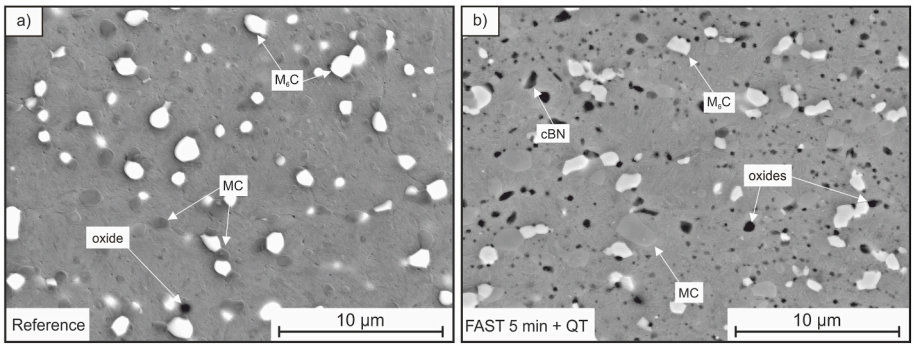


Fig. 10. Exemplary SEM images in SE contrast of a) the PM T15 reference material and b) the FAST 5 min + QT sample.

investigated. These properties are compared to the reference material.

3.4.1. Static compression testing

Compression tests were carried out to investigate the influence of the contaminants on the static mechanical properties. The resulting compressive yield strength, the ultimate compressive strength, and the fracture strain, as well as the hardness, are shown in Table 3.

The static mechanical properties of both materials exhibit a high degree of similarity. The compressive yield strength of the FAST 5 min + QT sample was only 7 % below that of the reference material. Both states achieved ultimate compressive strengths of more than 4000 MPa, and the ultimate compressive strength of the FAST state was observed to be less than 10 % below that of the reference state. This is due to the spherical shape of the carbides, which provides advantages in terms of toughness [41]. Moreover, Table 3 shows that the fracture strain of the reference is 4 % above the strain in the FAST 5 min + QT sample when the fracture occurs. The compression specimens exhibited brittle fracture in both states.

The slight discrepancy between the static mechanical properties of the reference and the FAST 5 min + QT sample of PM T15 can be attributed to microstructural characteristics. As the difference between the reference material and the FAST 5 min + QT sample is small, the non-metallic inclusions appear to have almost no influence on the static mechanical properties. The FAST 5 min + QT sample exhibits a relative density of 99.63 %, from which it can be concluded that some residual porosity remains after sintering. The incomplete fusion of the particles during sintering due to oxide formation at the former chip surfaces slightly reduce the load-bearing cross-section of the compression specimens [42].

In contrast, the cold-worked steel grinding waste investigated by Groβwendt et al., which was compacted by electric discharge sintering, showed a lower degree of agreement in ultimate compressive strength between the recycled and reference materials, due to the presence of strong oxide deposits from a water-based cooling lubricant [18]. An oil-based cooling lubricant, as considered in this work, is therefore beneficial for the later mechanical properties, as this can prevent strong oxidation of the chips.

3.4.2. Cyclic pressure swelling testing

Pressure swelling tests were performed to determine the stress in correlation with the number of cycles up to a crack formation. Following the pressure swelling tests, all samples were examined by SEM to detect incipient cracks. The related curves of the reference material and the FAST 5 min + QT state are shown in Fig. 11.

A distinction between the recycled and the reference material is recognizable, particularly within the range of $1 \cdot 10^4$ to $6 \cdot 10^5$ cycles (Fig. 11). Below a stress level of 140 MPa, both materials exhibited no formation of cracks up to a number of $1 \cdot 10^7$ load cycles (Fig. 11).

Fig. 12 shows the FAST 5 min + QT state and the reference material after 50,000 cycles at 230 MPa. In the SEM image of the reference material, a small incipient crack with a length of about 20 µm could be determined (Fig. 12a and b). In contrast, the incipient crack in the FAST 5 min + QT sample was 40 times longer (~800 µm) (Fig. 12c). An incipient crack starts with plastic flow in a larger material volume. The formation of a plastic zone is reduced in the case of rather brittle materials. As a result, stress overloads occur more quickly on more resistant barriers, such as non-metallic inclusions or carbides. This consequently leads to a failure in the material exhibiting the highest local residual stress [43]. Fig. 12c and d display the formation of an incipient crack in the FAST 5 min + QT sample. Fig. 12d shows the crack propagation of the incipient crack. Depicted is a broken and partly detached sharp-edged Al_2O_3 particle which is in the crack path and broke due to local high stresses at the crack tip. In addition to the size of the non-metallic inclusions or carbides, the shape of the particles created an additional notch effect, which has a negative impact on crack formation and crack growth (compare Table 2) [44]. Lueg et al. described that the

Table 3
Static mechanical properties of the reference material and the FAST 5 min + QT recyclate of PM T15.

	Compressive yield strength in MPa	Ultimate compressive strength in MPa	Fracture strain in %
Reference	4012 ± 82	4543 ± 194	13.75 ± 1.6
FAST 5 min + QT	3744 ± 66	4261 ± 102	9.75 ± 0.4

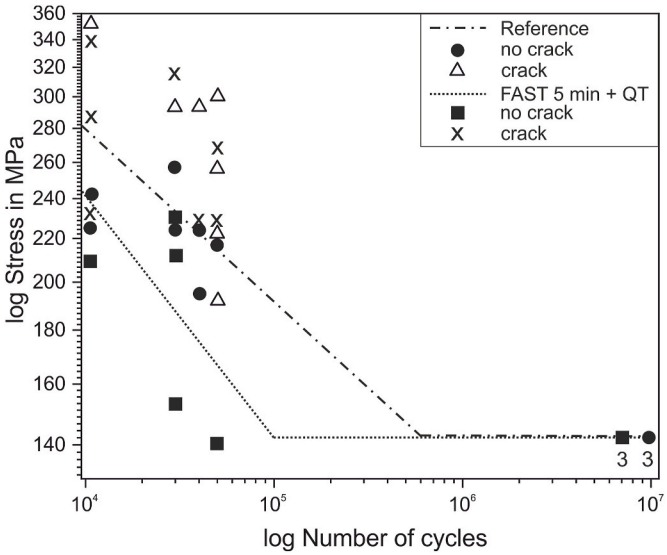


Fig. 11. Pressure swelling test: Correlation curve of stress and number of cycles until formation of an incipient crack. Three specimens of each state were tested under a stress of 140 MPa.

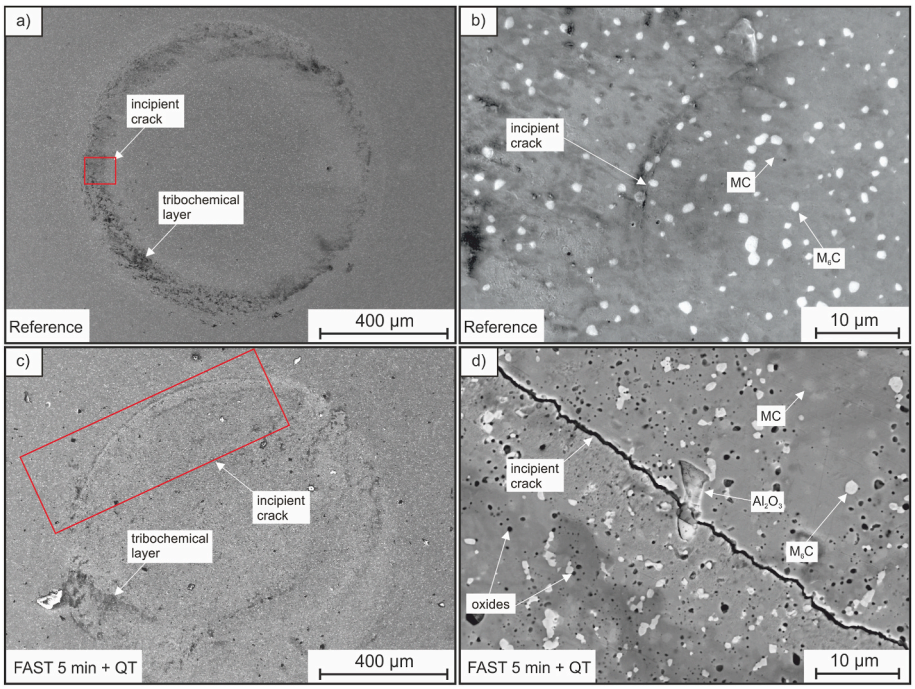


Fig. 12. Pressure swelling test: SEM images in SE contrast of the reference material and FAST 5 min + QT recyclate: a) and c) overview of incipient crack, and b) and d) incipient crack path at high magnification at stress of 230 MPa and 50,000 load cycles.

fatigue crack initiation generally starts at the length of the largest discontinuity normal to the applied stress [45]. This explains the fact, that the FAST 5 min + QT sample exhibited crack formation at a lower stress level in the low-cycle fatigue range, as it was contaminated with large and sharp-edged Al_2O_3 particles (compare Table 2) [46].

Following the crack path, there was little influence on the crack propagation from surrounding large abrasives and oxide formations in the FAST 5 min + QT sample. The incipient crack of the FAST 5 min + QT sample had continued in its path defined by the circular stress field caused by the geometry of the spherical indenter. It was not deflected by the large surrounding abrasive particles. But if the abrasives and oxides were in the defined propagation path, it can be determined that either the abrasives were separated, or the crack grew along the larger oxides (Fig. 12d). A significant influence on crack formation and propagation of the smaller abrasives cBN and the small oxides could not be found.

3.4.3. *Cyclic three-point bending testing*

Cyclic three-point bending tests on single edge notched bending (SENB) samples were performed to investigate the potential influence of non-metallic inclusions and carbides on the crack propagation rate. The crack propagation starts at the Chevron-notch where a crack gage was mounted. Fig. 13 illustrates the growth rate da/dN of the fatigue crack in correlation with the cyclic stress intensity factor ΔK in specimens taken from the reference material and the FAST 5 min + QT sample. The samples of the reference material were extracted so that the crack runs perpendicular to the rolling direction (compare Fig. 2).

The threshold of the stress intensity ΔK_{th} of both states was measured to be 4.1 MPa $\cdot\sqrt{}$ m. Due to the well-adapted heat-treatment of the FAST 5 min + QT sample, the properties of the metal matrix could match those of the reference material. As a result, the fracture resistance of the metal matrix during crack growth from one hard phase to a neighboring one is approximately equivalent. This enabled the same threshold value to be achieved as in the reference material.

The interparticle distance between the carbides in the FAST 5 min + QT sample is slightly larger, compared to the reference material (Table 2). However, the mean free matrix path is reduced through additional abrasives and oxides (compare Table 2).

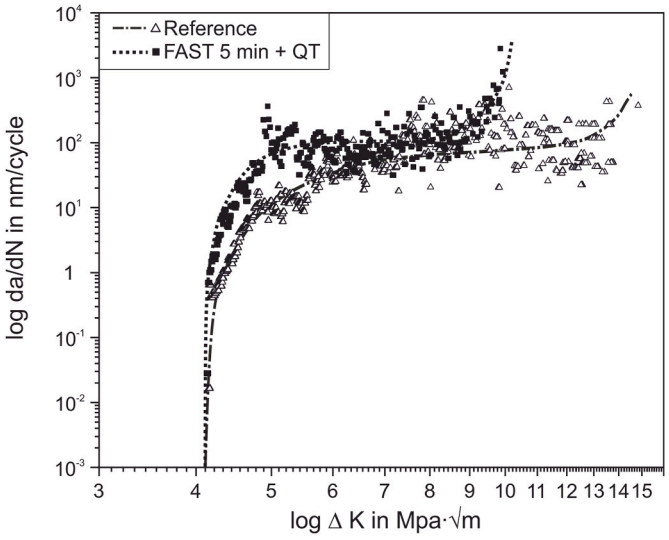


Fig. 13. Cyclic three-point bending test: Growth rate da/dN of the fatigue crack of the reference material and the FAST 5 min + QT recyclate.

The influence of microstructural features on crack propagation was investigated by SEM (Fig. 14). Fig. 14a and b show the crack path in a specimen of the reference material. A visual comparison of the crack path in the FAST 5 min + QT sample with the reference material reveals a high degree of similarity (Fig. 14b and d). The crack path in both samples transitioned through the matrix, intergranular along the interface between matrix and carbides, or transgranular through a carbide (M_6C). In both materials, carbides of type MC remained intact, causing crack propagation along the interface between carbide and metal matrix, whereas the carbides of type M_6C were fractured (Fig. 14b and d). This phenomenon can be attributed to the higher elastic modulus of the MC, which contributes to a higher strength and fracture toughness [35]. In both materials, the propagation of the crack was almost linear, and

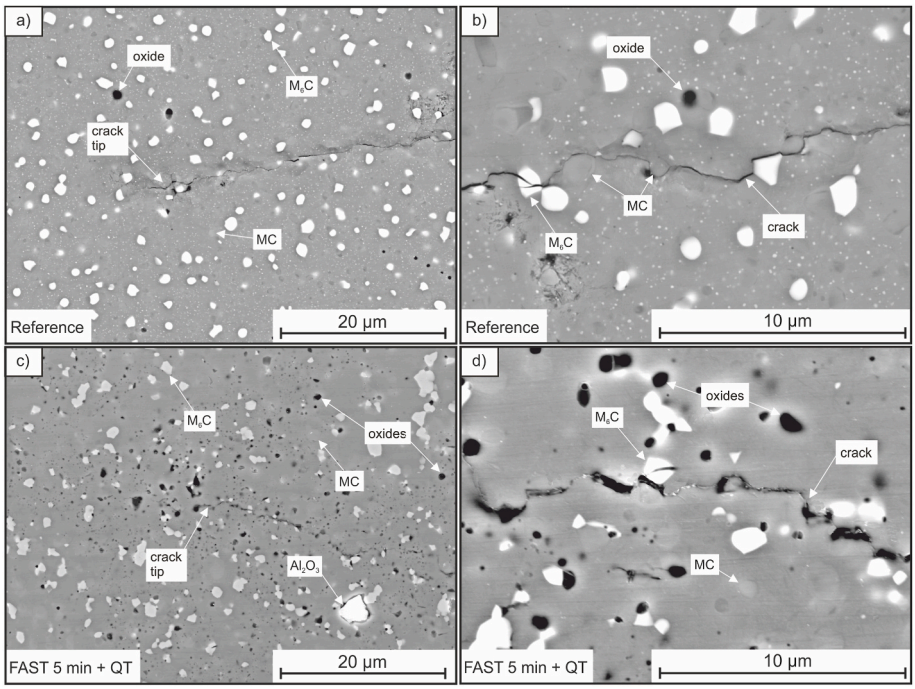


Fig. 14. Micrographs in SE-contrast of the SENB samples after cyclic three-point bending testing: a) crack tip and b) crack path of the reference material, as well as c) crack tip and d) crack path of the FAST 5 min + QT sample. The direction of crack propagation was from right to left.

the crack did not branch to adjacent abrasive particles in the FAST 5 min + QT sample. As mentioned in section 3.4.23.4.2, the presence of large Al_2O_3 inclusions near the crack path exhibited no pronounced influence on the crack path (Fig. 14c).

The crack propagation acceleration for steels with a similar chemical composition (compare Table 1) depends on the heat-treatment and the production process [47]. The same heat-treatment (QT) was applied to both materials, resulting in a similar microstructure (matrix and carbides) (Fig. 10). The manufacturing process differed significantly, resulting in the FAST 5 min + QT sample being contaminated with additional oxides and abrasives. Even a few large detached non-metallic inclusions can lead to large crack expansions, especially if the crack growth through the matrix is still very slow due to the low ΔK [48]. The tendency for carbides with a high degree of sphericity and small size like carbides of type MC and M_6C to debond from the metal matrix is documented in Fig. 14. Conversely, hard phases with a high aspect ratio and large size like the Al_2O_3 particles are more likely to fracture (Fig. 12d) [44]. Thus, the growth rate da/dN of the fatigue crack of the FAST 5 min + QT sample increases significantly faster (Fig. 13).

Detached carbides and oxides, which are responsible for the formation of secondary cracks, can be observed in the vicinity of the crack (Fig. 14b and d). The surrounding carbides extract energy from the main crack by promoting the formation of secondary cracks, thereby retarding further growth. This phenomenon is referred to as “crack tip shielding“ [37]. However, the presence of the brittle and not metallurgically bonded Al_2O_3 can as well accelerate crack growth through fracturing.

The transition to the Paris regime is characterized by the decreasing influence of the microstructure, which results in a linear relationship between the crack growth rate and the stress intensity in the double-logarithmic plot [49].

The recycled specimens produced by FAST transition towards unstable crack growth at lower ΔK, which can be explained by the increasing proportion of low-energy cleavage fracture. The higher content of abrasives and oxides in the FAST 5 min + QT sample causes a lower mean free matrix path (Table 2), which facilitates the low-energy cleavage fracture along the interface of carbides or oxides and the metal matrix, as well as transgranular fracture of the brittle phases. The higher mean free matrix path of the reference material contributes to an increased resistance against cleavage fracture, as the increased proportion of the crack path through the metal matrix is associated with higher crack energy dissipation [44]. Thus, the transition to the unstable crack growth occurs at higher ΔK in the reference material (Fig. 13).

3.5. Application of the FAST-recyclate

A cutting disc with an outer dimension of 120 mm (Fig. 2) was successfully fabricated via FAST using recycled PM T15 grinding chips and was tested for 20 min on a mechanized tunneling test rig under constant conditions (Fig. 3). Compared to the reference, the recycled material showed a reduced durability. Crack propagation was identified as the dominant damage mechanism, ultimately leading to breakout failures. Breakouts from the cutting disc indicate delamination, pointing to low fracture toughness. Overrolling further accelerated crack growth (Fig. 15c).

As discussed in the prior sections, a major factor contributing to the observed damage is the short free matrix path length, caused by oxide layers between individual chips – especially along the chip orientation (Table 2 and Fig. 10b). These oxide interfaces act as preferred pathways for crack initiation and fast propagation. Cracks were found to grow predominantly along these boundaries. A SEM analysis in Fig. 15d confirmed that delamination cracks follow the material's layered structure, which corresponds to the alignment of the original chip shapes.

During operation, the cutting edge of the recycled cutting disc can be seen as resharpened, resulting in a narrower geometry and increased Hertzian pressures but a lower durability. The resharpening lead to the phenomenon, that the recycled disc excavated almost twice as much rock then the disc made from the reference material (424 g/219 g). However, in turn, the reference material did not show any macroscopic or microscopic damage after the trial (Fig. 15a and b). This superior durability is attributed to a longer matrix path length and the absence of significant oxide inclusions (Table 2 and Fig. 10a). As a result, there were no continuous weak interfaces along which cracks could propagate, which significantly enhanced the material's resistance to damage under the same loading conditions.

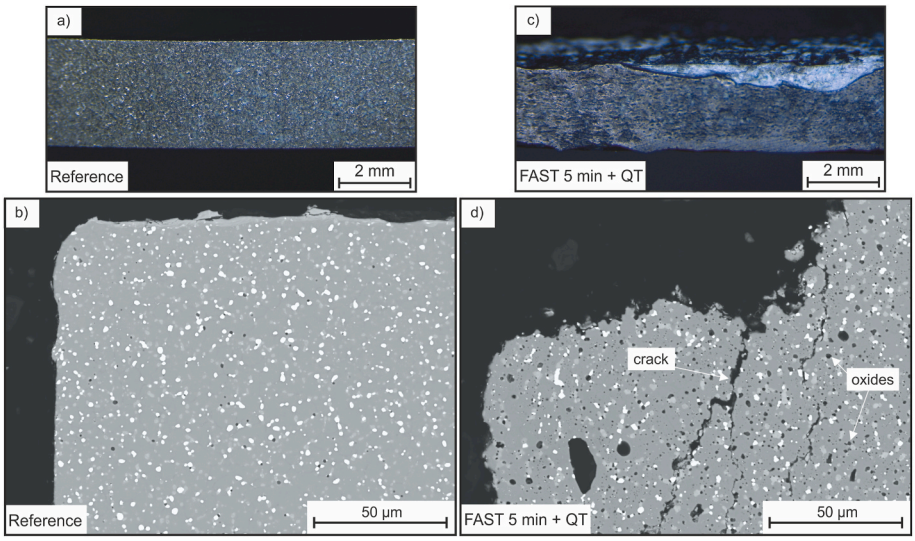


Fig. 15. a) and c) Photographs and b) and d) SEM images in BSE contrast of the cutting edges of the reference and the FAST-recyclate material after the test under mechanized tunneling conditions.

4. Conclusion

In this study, a strategy for direct recycling of PM T15 high-speed tool steel grinding waste using a powder metallurgical processing route was examined. For this purpose, the metallic grinding chips were first separated from the lubricant oil by washing and from the abrasives by vacuum filtration. Subsequently, the spiral and sickle shape of the grinding chips were almost eliminated by ball milling. After the preparation, the metallic chips were sintered by the innovative short-time field-assisted sintering technology "FAST". FAST has the advantage that powders can be compacted that would otherwise be difficult to process, for example, due to an unfavorable shape.

By cleaning the grinding waste, the C content and the abrasive content could be significantly minimized. Nevertheless, increased C contents (1.77 mass%) and remaining abrasive particles (0.2 vol%) were observed within the FAST-densified cutting discs. A density of 99.63 % was realized by sintering the chips at 950 °C and 45 MPa for 5 min.

After austenitizing at reduced temperature to compensate for the C uptake and tempering in the regime of secondary hardness, the retained austenite content of the FAST 5 min + QT sample could be reduced to a level comparable to the reference material and a similar hardness of almost 900 HV30 resulted. Analogous static mechanical properties of the FAST 5 min + QT sample compared to the reference material were achieved due to similar heat-treatments and resulting microstructures.

However, the Al_2O_3 particles are not well metallurgically bonded with the steel matrix and additional oxidized grinding chip surfaces impaired the cyclic mechanical properties and the performance in the mechanized tunneling test rig of the FAST-recycled high-speed tool steel.

In summary, to produce a material from the grinding chips that exhibits similar strength and toughness as material produced from pristine steel powder, the contaminations of abrasives (especially Al_2O_3), oxidation, and residual oil must be decreased to a minimum.

A reduction in the abrasive content, especially of large and sharp-edged Al_2O_3 particles, and the adhering cooling lubricants is necessary to bring the properties of the recycled material into line with those of the reference material. The abrasives lead to an inhomogeneous microstructure and sharp-edged non-metallic inclusions lead to stress exaggeration. But the shortened free matrix path due to Al_2O_3 particles can also be advantageous for an application where wear protection is required [3]. A possible process to decrease the content of abrasives is additional sifting of the grinding waste.

In the case of residual oil content, oil evaporation might result in an expansion of the existing pores during FAST compaction especially at higher temperatures. To exclude this influence, the residual oil content can be – after the usual washing of the grinding waste with liquid media – further reduced by supercritical CO_2 extraction or vacuum evaporation subsequent to a pre-deoiling step like centrifugation. This could have a noticeable effect on the initial carbon content and hydrogen embrittlement which can affect the mechanical materials' behavior.

In addition, to weaken the impact of contaminations, the grinding chips can be optionally mixed with pristine gas atomized powder. Thereby, at least a part of the required primary raw materials could be saved [20].

Funding

The author would like to thank the german federal ministry for economics and energy (BMWE) for funding the project GENESIS – Ener**G**ieeffizi**ENtE** Krei**S**laufwirtschaft kr**I**tischer Roh**S**toffe [grant number 03EI5009]. Besides the author would like to thank Prof. Kathrin Greiff of RWTH Aachen for providing resources regarding the preparation of the starting material.

Declaration of competing interest

The authors declare that they have no known competing financial interests or personal relationships that could have appeared to influence the work reported in this paper.

Appendix 1

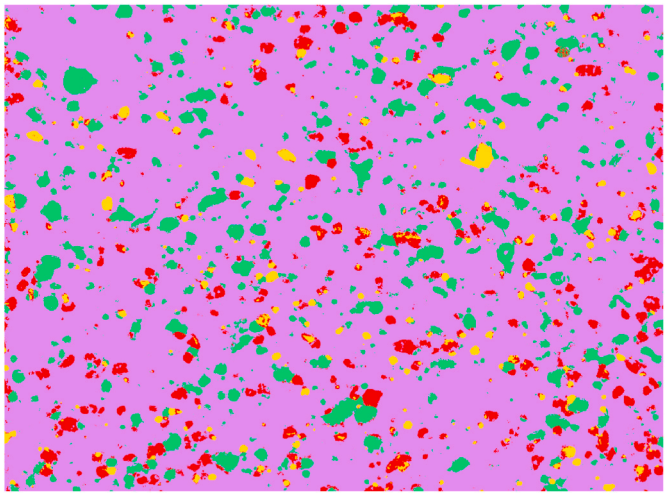


Fig. 16. Example of a processed image of FAST 5 min + QT at 5,000x magnification for determination of volume fraction, sizes and aspect ratio of various precipitates. The matrix is highlighted in purple, the M_6C in green, the MC in red, and the oxides in yellow.

References

[1] Nuss P, Harper EM, Nassar NT, Reck BK, Graedel TE. Criticality of iron and its principal alloying elements. Environmental Science & Technology 2014;48(7):4171–7. https://doi.org/10.1021/es405044w.

[2] Nygaard A. The geopolitical risk and strategic uncertainty of green growth after the Ukraine invasion: how the circular economy can decrease the market power of and resource dependency on critical minerals. Circ Econ Sust 2023;3(2):1099–126. https://doi.org/10.1007/s43615-022-00181-x.

[3] Eifert H, Veltl G, Rickel J, Eckebrecht J, Schulz A. Pulvermetallurgie von Schleifschlämmen: Schleifschlamm als mögliche neue Quelle für Metallpulver. Metalloberfläche - beschichten von Kunststoff und Metall 50. IGT; 1996.

[4] Hu X, Wang C, Lim MK, Koh SCL. Characteristics and community evolution patterns of the international scrap metal trade. J Clean Prod 2020;243:118576. https://doi.org/10.1016/j.jclepro.2019.118576.

[5] Medeiros ES, Polk A. China's new economic weapons. Wash Q 2025;48(1):99–123. https://doi.org/10.1080/0163660X.2025.2480513.

[6] Tönshoff HK, Westkämper E. Yearbook grinding honing, lapping, polishing. Essen. Germany: Vulkan-Verlag Essen; 1997.

[7] Großwendt F, Keszler M, Weber M, Bram M, Weber S. Zirkuläre Wertschöpfung hochlegierter metallischer Reststoffe durch pulvermetallurgische Methoden. Jülich: Forschungszentrum; 2023.

[8] Teubler J, Weber S, Suski P, Peschke I, Liedtke C. Critical evaluation of the material characteristics and environmental potential of laser beam melting processes for the additive manufacturing of metallic components. J Clean Prod 2019;237:117775. https://doi.org/10.1016/j.jclepro.2019.117775.

[9] Brinksmeier E, Eckebrecht J, Buhr H. Improving ecological aspects of the grinding process by effective waste management. J Mater Process Technol 1994;44(3):171–8. https://doi.org/10.1016/0924-0136(94)90429-4.

[10] Allwood JM, Ashby MF, Gutowski TG, Worrell E. Material efficiency: a white paper. Resour Conserv Recycl 2011;55(3):362–81. https://doi.org/10.1016/j.resconrec.2010.11.002.

[11] Blengini GA, Latunussa CE, Eynard U, Matos CT de, Wittmer D, Georgitzikis K, et al. Study on the EU's list of critical raw materials. Final Report. Publications Office of the European Union; 2020. 2020.

[12] Månberger A, Johansson B. The geopolitics of metals and metalloids used for the renewable energy transition. Energy Strategy Rev 2019;26:100394. https://doi.org/10.1016/j.esr.2019.100394.

[13] United Nations. A/RES/70/1. Transforming our world: the 2030 agenda for sustainable development, vol. 22. New York, NY, USA: United Nations; 2015. p. 24.

[14] Singh A, Singh Dhami H, Kumar Sinha M, Kumar R. Evaluation and comparison of mineralogical, micromeritics and rheological properties of waste machining chips, coal fly ash particulates with metal and ceramic powders. Powder Technol 2022;408:117696. https://doi.org/10.1016/j.powtec.2022.117696.

[15] Keszler M, Grosswendt F, Assmann A-C, Krengel M, Maccari F, Gutfleisch O, et al. Direct recycling of hot-deformed nd–fe–b magnet scrap by field-assisted sintering technology. Adv Energy Sustain Res 2024;5(1):2300184. https://doi.org/10.1002/aesr.202300184.

[16] Canakci A, Varol T. A novel method for the production of metal powders without conventional atomization process. J Clean Prod 2015;99:312–9. https://doi.org/10.1016/j.jclepro.2015.02.090.

[17] Fu H, Matthews MA. Separation processes for recovering alloy steels from grinding sludge: supercritical carbon dioxide extraction and aqueous cleaning. Separ Sci Technol 1999;34(6–7):1411–27. https://doi.org/10.1080/01496399908951100.

[18] Großwendt F, Bürk V, Kopanka B, Jäger S, Pollak S, Leich L, et al. A novel powder-metallurgical eco-friendly recycling process for tool steel grinding sludge. J Clean Prod 2023;392:136329. https://doi.org/10.1016/j.jclepro.2023.136329.

[19] Grosso M, Motta A, Rigamonti L. Efficiency of energy recovery from waste incineration, in the light of the new waste framework directive. Waste Management 2010;30(7):1238–43. https://doi.org/10.1016/j.wasman.2010.02.036.

[20] Jäger S, Weber S, Röttger A. Potential of the recycling of grinding sludge by various powder metallurgical processes. Proced CIRP 2021;104:893–9. https://doi.org/10.1016/j.procir.2021.11.150.

[21] Yoshimura T, Thotsaphon T, Imai H, Kondoh K. Microstructural and mechanical properties of Ti composite reinforced with TiO2 additive particles. Trans JWRI 2009;38(2):37–41.

[22] Weston NS, Jackson M. FAST-Forge of titanium alloy swarf: a solid-state closed-loop recycling approach for aerospace machining waste. Metals 2020;10(2):296.

[23] Musa C, Licheri R, Locci AM, Orrù R, Cao G, Rodriguez MA, et al. Energy efficiency during conventional and novel sintering processes: the case of Ti–Al2O3–TiC composites. J Clean Prod 2009;17(9):877–82. https://doi.org/10.1016/j.jclepro.2009.01.012.

[24] Mamedov V. Spark plasma sintering as advanced PM sintering method. Powder Metall 2002;45(4):322–8. https://doi.org/10.1179/003258902225007041.

[25] Munir ZA, Anselmi-Tamburini U, Ohyanagi M. The effect of electric field and pressure on the synthesis and consolidation of materials: a review of the spark plasma sintering method. J Mater Sci 2006;41(3):763–77. https://doi.org/10.1007/s10853-006-6555-2.

[26] Anthroprogene Stoffkreisläufe, RWTH Aachen University. Metallischer schleifschlamm. Circular Material Database. [July 04, 2025]; Available from: https://circulated.rwth-aachen.de/index.php?title=Metallischer_Schleifschlamm.

[27] Guillon O, Gonzalez-Julian J, Dargatz B, Kessel T, Schierning G, Räthel J, et al. Field-assisted sintering technology/spark plasma sintering: mechanisms, materials, and technology developments. Adv Eng Mater 2014;16(7):830–49. https://doi.org/10.1002/adem.201300409.

[28] DIN EN ISO 6507-1:2018-07, Metallische Werkstoffe - Härteprüfung nach Vickers - teil 1: prüfverfahren (ISO 6507-1:2018). Berlin: Beuth-Verlag.

[29] DIN 50106:2016-11, Prüfung metallischer Werkstoffe - Druckversuch bei Raumtemperatur. Berlin: Beuth-Verlag.

[30] Abudaia FB, Evans JT, Shaw BA. Spherical indentation fatigue cracking. Mater Sci Eng 2005;391(1):181–7. https://doi.org/10.1016/j.msea.2004.08.068.

[31] E08 Committee. Test method for measurement of fatigue crack growth rates(e 647 - 15). West Conshohocken, PA: ASTM International; 2015. https://doi.org/10.1520/E0647-15.

[32] Brackmann L, Röttger A, Treppmann M, Weber S. The behavior of cutting discs for mechanized tunneling under cyclic loading conditions. Tunn Undergr Space Technol 2023;137:105151. https://doi.org/10.1016/j.tust.2023.105151.

[33] Benito S, Wulbieter N, Pöhl F, Theisen W. Microstructural analysis of powder metallurgy tool steels in the context of abrasive wear behavior: a new computerized approach to stereology. J Mater Eng Perform 2019;28(5):2919–36. https://doi.org/10.1007/s11665-019-04036-9.

[34] Keszler M, Großwendt F, Weber S, Guillon O, Bram M. Direct recycling of tool steel swarf using field assisted sintering. Proceedings of 2024 Powder Metallurgy World Congress & Exhibition. 2024. p. 766–73.

[35] Randall NX, Vandamme M, Ulm F-J. Nanoindentation analysis as a two-dimensional tool for mapping the mechanical properties of complex surfaces. J Mater Res 2009;24(3):679–90. https://doi.org/10.1557/jmr.2009.0149.
[36] Lima E, das Neves MDM, Nogueira RA, Oliveira L de, Ambrozio Filho F. Effect of different tempering stages and temperatures on microstructure, tenacity and hardness of vacuum sintered HSS AISI T15. Inside MS 2008;591–593:68–73. https://doi.org/10.4028/www.scientific.net/MSF.591-593.68.
[37] Lentz J, Röttger A, Theisen W. Solidification and phase formation of alloys in the hypoeutectic region of the Fe–C–B system. Acta Mater 2015;99.
[38] Ghomashchi MR, Sellars CM. Microstructural changes in As-Cast M2 grade high speed steel during hot forging. Metall Trans A 1993;24(10):2171–80. https://doi.org/10.1007/BF02648591.
[39] Chaus AS, Maksimenko AV, Fedosenko NN, Čaplovič Ľ, Myshkovets VN. Formation of structure of a high-speed steel upon laser surface melting. Phys Met Metall 2019;120:269–77.
[40] Niederhofer P, Eger K, Schwingenschlögl P, Merklein M. Properties of tool steels for application in hot stamping. steel research int 2020;91(5):1900422. https://doi.org/10.1002/srin.201900422.
[41] Mesquita RA, Barbosa CA. High-speed steels produced by conventional casting, spray forming and powder metallurgy. Mater Sci Forum 2005;498–499:244–50. https://doi.org/10.4028/www.scientific.net/MSF.498-499.244.
[42] Simchi A, Danninger H. Electrical conductivity and microstructure of sintered ferrous materials: sintered iron. Powder Metall 2000;43(3):209–18. https://doi.org/10.1179/003258900665961.
[43] Berns H. Crack initiation and growth in tool Steels.(Retroactive coverage). Fatigue 90; 1990. p. 161–6.
[44] Brackmann L, Wingender D, Weber S, Balzani D, Röttger A. Influence of hard phase size and spacing on the fatigue crack propagation in tool steels—Numerical simulation and experimental validation. Fatig Fract Eng Mater Struct 2023;46(10):3872–91. https://doi.org/10.1111/ffe.14107.
[45] Berns H, Lueg J, Trojahn W, Wahling R, Wisell H. The fatigue behaviour of conventional and powder metallurgical high speed steels. Powder Metall Int 1987;19(4):22–6.
[46] Thornton PA. The influence of nonmetallic inclusions on the mechanical properties of steel: a review. J Mater Sci 1971;6(4):347–56. https://doi.org/10.1007/PL00020378.
[47] Suresh S, Ritchie RO. Propagation of short fatigue cracks. Int Met Rev 1984;29(6).
[48] Schwalbe K-H. On the influence of microstructure on crack propagation mechanisms and fracture toughness of metallic materials. Eng Fract Mech 1977;9(4):795–832. https://doi.org/10.1016/0013-7944(77)90004-2.
[49] Ritchie RO. Near-threshold fatigue-crack propagation in steels. Int Met Rev 1979;24(1).